Geoscientific Model Development Discussions

Open Access

Application and evaluation of McICA scheme with new radiation code in BCC_AGCM2.0.1

H. Zhang[1,2], X. Jing[1], and J. Li[3]

[1]Laboratory for Climate Studies, National Climate Center, China Meteorological Administration, Beijing, China
[2]Nanjing University of Information Science and Technology, Nanjing, China
[3]Canadian Center for Climate Modeling and Analysis, University of Victoria, Victoria, British Columbia, Canada

Correspondence to: H. Zhang (huazhang@cma.gov.cn)

Discussion Paper | Discussion Paper | Discussion Paper | Discussion Paper |

GMDD
6, 4933–4982, 2013

Application and evaluation of McICA scheme

H. Zhang et al.

Title Page

Abstract   Introduction
Conclusions   References
Tables   Figures

◄◄   ►►
◄   ►

Back   Close

Full Screen / Esc

Printer-friendly Version
Interactive Discussion

Abstract

This research incorporates the Monte Carlo Independent Column Approximation (McICA) scheme with the correlated k-distribution BCC-RAD radiation model into the climate model BCC_AGCM2.0.1 and examines the impacts on modeled climate through several simulations with variations in cloud structures. Results from experiments with consistent sub-grid cloud structures show that both clear-sky radiation fluxes and cloud radiative forcings (CRFs) calculated by the new scheme are mostly improved relative to those calculated from the original one. The modeled atmospheric temperature and specific humidity are also improved due to changes in the radiative heating rates.

The vertical overlap of fractional clouds and horizontal distribution of cloud condensation are important for computing CRFs. The maximum changes in seasonal CRF using the general overlap assumption (GenO) with different decorrelation depths (L_{cf}) are larger than 10 and 20 Wm^2 for longwave (LW) CRF and shortwave (SW) CRF, respectively, mostly located in the Tropics and mid-latitude storm tracks. Larger (smaller) L_{cf} in the Tropics (mid-latitude storm tracks) yield better cloud fraction and CRF compared with observations. The inclusion of an observation-based horizontal inhomogeneity of cloud condensation has a distinct impact on LW CRF and SW CRF, with global means of ~ 1.2 Wm^{-2} and ~ 3.7 Wm^{-2} at the top of atmosphere, respectively, making these much closer to observations.

These results prove the reliability of the new model configuration to be used in BCC_AGCM2.0.1 for climate simulations, and also indicate that more detailed real-world information on cloud structures should be obtained to constrain cloud settings in McICA in the future.

1 Introduction

Clouds are critically important in modulating the radiation budget of the earth–atmosphere system. The representation of clouds and cloud-radiation feedback contributes the greatest uncertainty to simulations of general circulation models (GCMs) (IPCC, 2007). This arises mostly from the relatively coarse spatial resolution of GCMs (dozens to hundreds of kilometers), which leaves cloud-relevant processes and the inherent sub-grid variations of clouds unresolved (Barker and Räisänen, 2005; Zhang et al., 2013a).

Typically, cloud condensation (water and ice) is treated as horizontally homogeneous (the plane parallel homogeneous, or PPH, assumption) within a GCM grid cell. Additionally, certain predetermined assumptions about the vertical overlap of fractional clouds are required. However, both the PPH and overlap treatments are inefficient for producing accurate radiation flux and heating rates and thus bring enormous biases to climate responses. The PPH assumption can easily overestimate the radiative fluxes at the top of the atmosphere (TOA) and the surface by dozens or even > 100 W/m^2 and produce heating rate errors, often more than 30 % (Cahalan et al., 1994; Oreopoulos and Davies, 1998). The widely used max-random or random overlap assumption yields even more radiative flux errors than does PPH (Barker et al., 1999). Stephens et al. (2004) showed that other climate variables, such as surface temperature and water vapor, suffer severely from biases in sub-grid cloud structures. All of these studies have emphasized the importance of faithfully addressing sub-grid cloud variability in GCMs.

One of the solutions to this problem is to develop high-resolution cloud-resolving models. However, this is currently too computationally expensive for operational use considering the computer speeds available today. Therefore, more attempts are being made toward statistically precise parameterizations for the representation of clouds in GCMs. Abundant approaches for handling parameterization of sub-grid clouds in GCMs have been developed. These include the "tripleclouds" scheme (Shonk and Hogan, 2008), the mosaic treatment (Liang and Wu, 2005), and the multi-column

Full Screen / Esc

Printer-friendly Version

Interactive Discussion

(Stubenrauch et al., 1999) and quasi-column approaches (Li et al., 2005). However, most of these approaches are highly embedded in their radiation transfer codes. The twisting of cloud structure description and radiative transfer causes them to lack the flexibility required to adjust to updated observational results or other transplanted radiation codes.

To make representation of sub-grid cloud properties flexible and modularized and to maintain computational efficiency, a new scheme, the Monte Carlo Independent Column Approximation (McICA) method, was developed (Pincus et al., 2003). It uses a sophisticated stochastic sub-grid cloud generator (hereafter SCG) (Räisänen et al., 2004) to explicitly obtain cloud subcolumn structures according to certain rules that constrain cloud overlap and horizontal distribution. Moreover, McICA also uses the spectral integration method to reduce computing time by reducing the full ICA (independent column approximation) approach through a Monte Carlo selection of subcolumns (Pincus et al., 2003). The advantages of McICA greatly facilitate adjustment or alteration of both cloud structure and radiative transfer and thus accelerate future development of GCMs.

Because of the advantages of the McICA scheme for treating the sub-grid cloud-radiation process, we here incorporate the McICA scheme into the Beijing Climate Center's general circulation model BCC_AGCM2.0.1 with the BCC-RAD radiation algorithm, which is based on the advanced correlated k-distribution (CKD) (Zhang et al., 2003, 2006a, b). CKD code is included to fulfill the requirement of spectral integration of McICA, to which the original band model is not applicable. Previous work has shown that the BCC_AGCM2.0.1 model, similar to other GCMs, is generally insensitive to McICA noise and that the performance of the model depends only on its own physics and dynamics (Jing and Zhang, 2013). Hence, the McICA scheme may possibly be applied for future development of BCC_AGCM2.0.1.

For this purpose, the current research evaluates climate simulation with the application of McICA and our radiation scheme BCC-RAD in BCC_AGCM2.0.1, specifically for investigating radiation and cloud-related fields. First, we analyze the differences in radiation budgets, surface climatology, and atmospheric states between the new and

old model configurations. Second, the impacts of the changes in the radiation scheme, cloud overlap assumption, and cloud-water inhomogeneity on the radiation budget and simulated climate are discussed. This preliminary work preceding the availability of observation-based sophisticated cloud information also aims to archive the impact of
5　the modifications in the cloud-radiation process on simulated climate and the model response to these changes and thereby provide suggestions for future development.

　　Section 2 of this paper briefly describes the McICA scheme, the BCC_AGCM2.0.1 model, and the BCC-RAD radiation scheme. The design of the experiments is given in Sect. 3. Results of simulations with various model configurations are described in
10　Sect. 4, and a discussion and conclusions are presented in Sect. 5.

2　Model description

2.1　Description of the McICA scheme

The McICA scheme is based on the ICA algorithm for computation of domain mean radiation fields. It greatly and effectively reduces computation time while maintaining the
15　accuracy of ICA from a statistical perspective. The basic principles of McICA were first explained in detail by Pincus et al. (2003); Räisänen and Barker (2004) then provided additional ways to diminish induced noise. For clarity and completeness, we provide a brief summary here.

　　Conceive a domain R (a GCM grid). The sub-grid clouds could be represented by
20　a certain number of subcolumns, which contain individual cells in each layer that are either clear or overcast. Moreover, the domain mean of these subcolumns should hold the cloud profiles provided by the GCM. Given these subcolumns, radiative computation can be liberated from the description of partial clouds and their vertical overlap. The required subcolumns could be derived through SCG with consideration of cer-
25　tain overlap and horizontal distribution rules for clouds. For a thorough methodology of SCG, one can refer to Räisänen et al. (2004).

Within the domain R composed of subcolumns, the domain-averaged radiative fluxes can be accurately given by ICA as:

$$\left\langle F^{\text{ICA}} \right\rangle = \int S(\lambda) \left\{ \int \int_R F(x, y, \lambda) \, dx \, dy \right\} d\lambda \tag{1}$$

where x and y are subcolumn counters along the zonal and meridional axis, respectively, $S(\lambda)$ is the spectral weight at wavelength λ, and $F(x, y, \lambda)$ denotes the radiative flux at location (x, y) and wavelength λ.

If R is partially cloudy, $\left\langle F^{\text{ICA}} \right\rangle$ can be split into clear $\left\langle F^{\text{clr}} \right\rangle$ and cloudy $\left\langle F^{\text{cld}} \right\rangle$ parts weighted by the cloud fraction Ac:

$$\left\langle F^{\text{ICA}} \right\rangle = (1 - Ac) \left\langle F^{\text{clr}} \right\rangle + Ac \left\langle F^{\text{cld}} \right\rangle \tag{2}$$

The most time-consuming part of Eq. (2) is $\left\langle F^{\text{cld}} \right\rangle$ due to the full spectral integration in all cloudy subcolumns. To diminish the computational burden, Pincus et al. (2003) reduced the two-dimensional integration to a single dimension by introducing a Monte Carlo (random sampling) process:

$$\left\langle F^{\text{cld}} \right\rangle \approx \int S(\lambda) F^{\text{cld}}(s_{\text{rnd}}, \lambda) \, d\lambda \tag{3}$$

where s_{rnd} is a randomly selected cloudy subcolumn number for radiative calculation at λ. Equation (2) tremendously reduces computation time compared with Eq. (2) and represents the kernel of McICA.

It should be noted that the random selection of s_{rnd} in Eq. (2) inevitably introduces random noise. Although this may yield deviated results for a single calculation, averaging over a number of calculations generates almost unbiased results with respect to ICA (Barker et al., 2008). One method for reducing the noise is to increase the number

Full Screen / Esc

Printer-friendly Version

Interactive Discussion

of s_{rnd} for optically critical spectral intervals (Räisänen and Barker, 2004). To date, the McICA scheme has already been operationally utilized in several climate models and numerical weather prediction models (Morcorrete et al., 2008; Räisänen and Jarvinen, 2010; Neale et al., 2010).

2.2 Description of BCC_AGCM2.0.1

BCC_AGCM2.0.1 was developed by the Beijing Climate Center (BCC) at the China Meteorological Administration (CMA) based on the Community Atmosphere Model Version 3 (CAM3) of the National Center for Atmospheric Research (NCAR) (Wu et al., 2010). The model runs at T42 spectral resolution (approximately 2.8° × 2.8°) horizontally, and it uses vertical hybrid δ-pressure coordinates including 26 layers with the top located at about 2.9 hPa. An additional layer is added above the topmost layer in the radiative calculation to prevent excessive heating. The default timestep is 20 min, and the radiation code is invoked every three timesteps.

Relative to CAM3, several revisions have been made to improve the physics of the model. These include new reference atmosphere and surface pressures; a revised convection scheme (Zhang and Mu, 2005) that significantly improves the tropical rainfall simulation; a different function for calculating the snow-cover fraction that influences the resulting surface albedo, especially in polar and plateau regions (Wu and Wu, 2004); a new adiabatic adjustment originated by Yan (1987); and new methods for calculating turbulent fluxes over ocean surface that remove the systematic biases in the wind stress and sensible and latent heat fluxes in CAM3. A more detailed description of BCC_AGCM2.0.1 can be found in Wu et al. (2010). In the present research, the interactive Canadian Aerosol Module (CAM) (Gong et al., 2003) with updated aerosol emission sources (Zhou et al., 2012) is used to predict atmospheric aerosol burdens (Zhang et al., 2012).

2.3 Description of radiation schemes

To satisfy the requirement of the spectral integration of the McICA scheme, our radiation model, BCC-RAD, is adopted. This model is substantially different from the previous radiation scheme used in BCC_AGCM2.0.1. To explain the importance of this radiation scheme in modulating the climate simulation, it is necessary to describe this revision in advance. A detailed comparison between the old and new schemes is provided in Table 1.

The previous radiation scheme in BCC_AGCM2.0.1 is basically a band model. Although some band models simulated well the broadband fluxes and heating rates, this may have been partly fortuitous because of band overlap effects (Ellington et al., 1991). Another defect of band models is the use of a scaling procedure to account for inhomogeneous atmospheric paths, although these can be made arbitrarily accurate for a homogeneous atmosphere (Kratz, 1995). Therefore, there has been a trend over the past decades to replace band models with CKD methods in GCMs (Fu and Liou, 1992; Sun and Rikus, 1999; Nakajima et al., 2000; reference therein). As discussed in the introduction, the spectral information is needed in application of McICA.

In this work, we incorporate the CKD model by Zhang et al. (2003, 2006a, b), i.e., the Beijing Climate Center RADiation transfer model (BCC-RAD), into BCC_AGCM2.0.1 within the framework of McICA. The 10–49000 cm^{-1} (0.204–1000 μm) spectral range in BCC-RAD is divided into 17 bands (8 LW and 9 SW). Five major greenhouse gases (GHGs), H_2O, CO_2, O_3, N_2O, and CH_4, as well as chlorofluorocarbons (CFCs) are considered. The major absorbers in the solar bands are H_2O (including continuum absorption), CO_2, N_2O, O_3, and O_2. The HITRAN2000 database (Rothman et al., 2003) was used to provide line parameters and cross sections. Lu et al. (2012) compared the line parameters in different HITRAN versions and found that the difference in the simulated radiative fluxes between the updated HITRAN2008 and HITRAN2000 is very small, so the use of HITRAN2000 should not affect the final modeled climates in this research. In BCC-RAD, the effective absorption coefficients of CKD are calculated based

Title Page

Abstract | Introduction

Conclusions | References

Tables | Figures

|◄ | ►|

◄ | ►

Back | Close

Full Screen / Esc

Printer-friendly Version

Interactive Discussion

on the line-by-line radiative transfer model (LBLRTM; Clough and Iacono, 1995) with a spectral interval of 1/4 the mean half-width and a $25\,\mathrm{cm}^{-1}$ cutoff for line wings over each band (Clough and Iacono, 1995). The thermal radiation transfer calculation is solved with a two-stream algorithm developed by Nakajima et al. (2000), and the solar radiation transfer is solved with the δ-Eddington method (Coakley et al., 1983). SW radiation model comparisons, including BCC-RAD, are given in Randles et al. (2013).

Cloud and aerosol optical properties in BCC-RAD are also different from those in the original scheme. The optical properties of cloud droplets are from Nakajima (2000), and those of ice crystals are calculated based on several datasets: observational size distribution data from Fu (1996), optical properties of single particles of different shapes from Yang et al. (2005), and the fractional mixing of particles of various shapes suggested by Baum et al. (2005). Aerosol optical properties are from Wei and Zhang (2011) and Zhang et al. (2012).

3 Experimental design

We now have considered two model configurations, the new one with McICA and BCC-RAD to handle the cloud-radiative procedure and the old one with the traditional overlap treatment by Collins (2001) and radiation scheme described in Briegleb (1992). The details of these are listed in Table 1. Experiments were designed to reveal (a) the differences in simulated climate between the two configurations and (b) the impact of changing sub-grid cloud structures on simulated climate within the new configuration. All of the experiments are integrated with observed monthly distributions of SST from September 1979 to December 1990, and the results of the last 10 yr are used for analysis.

3.1 Experiments comparing the new and old model configurations

First, an experiment with the old scheme, denoted OLD, was performed as a control run. Second, two McICA experiments, a diagnostic offline (OL) run denoted NEW_MRO_OL and an interactive run denoted NEW_MRO, were conducted for comparison. Both the offline and interactive run utilized PPH and the max-random overlap (MRO) assumption (Tian and Curry, 1989) to be consistent with the OLD run. The NEW_MRO_OL and OLD simulations used identical atmospheric and cloud profiles for the cloud-radiation process; hence, the comparison between NEW_MRO_OL and OLD demonstrates the initial distinctions between the new and old configurations, whereas the comparison between NEW_MRO and OLD illustrates differences in the climate response.

3.2 Experiments exploring the impacts of sub-grid cloud structures

As the McICA scheme is flexible in depicting sub-grid cloud structures, four more experiments were implemented to test the model's sensitivity to cloud-structure variations.

First, the impact of changing cloud overlap was tested by including a so-called general overlap (hereafter GenO) (Mace and Benson-Troth, 2002). In GenO, the vertically projected cloud fraction of the two cloud layers k and l ($C_{k,l}$) is defined as the linear combination of maximum ($C_{k,l}^{max}$) and random overlap ($C_{k,l}^{ran}$):

$$C_{k,l} = \alpha_{k,l} C_{k,l}^{max} + \left(1 - \alpha_{k,l}\right) C_{k,l}^{ran} \tag{4}$$

where

$$C_{k,l}^{max} = \max(C_k, C_l) \tag{5}$$

$$C_{k,l}^{ran} = C_k + C_l - C_k C_l \tag{6}$$

and the overlap parameter $\alpha_{k,l}$ is prescribed via an exponential decay function of altitude separation between cloud layers:

$$\alpha_{k,l} = \exp\left[-\int_{z_k}^{z_l} \frac{dz}{L_{cf}(z)}\right] \qquad (7)$$

The lapse rate of the decay is controlled by a "decorrelation depth" (L_{cf} in Eq. 7), which has a global mean value of about 2 km (Barker, 2008) but it is highly related to cloud type and atmospheric dynamics (Naud et al., 2008). Zhang et al. (2013b) found that L_{cf} ranges, in terms of seasonal mean, within 0–3 km in different regions of East Asia. Thus, in this paper, three simulations with global constants L_{cf} of 1, 2, and 3 km, termed NEW_GO1, NEW_GO2, and NEW_GO3, respectively, were performed. Comparisons among NEW_GO1, NEW_GO2, NEW_GO3, and NEW_MRO will demonstrate the impact of changes in cloud overlap within the McICA scheme.

Additionally, the impact of breaking the default PPH assumption is addressed by perturbing the horizontal distribution of cloud condensation (water and ice) with an ideal distribution function. The gamma function of cloud condensation applied by Shonk et al. (2010) is used here. In such distribution, the magnitude of inhomogeneity is constrained by the fractional standard deviation (f), which is defined as:

$$f = \frac{\sigma_c}{\bar{c}} \qquad (8)$$

where $\bar{c}$ is the layer mean cloud condensation ignoring the cloud phase, and σ_c is the standard deviation of the condensation. In this work, f was set to 0.75 for both the liquid and ice phases, as was obtained by Shonk et al. (2010) from an extensive collection of observations. This inhomogeneity setting was tested in conjunction with GenO, with an L_{cf} of 2 km globally, denoted as NEW_GO2_IH. Because cloud vertical overlap assumptions are consistent between NEW_GO2 and NEW_GO2_IH, any discrepancies illustrate the impact of including horizontally inhomogeneous clouds.

Full Screen / Esc

Printer-friendly Version

Interactive Discussion

The simulated radiation fields, cloud fractions, and other climate variables were validated against corresponding observations or reanalysis data.

4 Results

This section reports the results of various simulations in three groups: (i) first, results from OLD, NEW_MRO_OL, and NEW_MRO are provided to clarify the differences between the new and old model configurations; (ii) second, results from NEW_MRO, NEW_GO1, NEW_GO2, and NEW_GO3 are presented to show the impact of cloud overlap variations within the scheme on radiation and other fields; and finally (iii) a comparison between NEW_GO2 and NEW_GO2_IH is given to show the influence of changing the horizontal distribution of cloud condensation on simulated climate.

4.1 Comparison between the new and old model configurations

4.1.1 Radiation budget

We first investigate the instantaneous difference between the old and new schemes under identical atmospheric and cloud conditions. Figure 1 shows the global annual mean radiation fields for various simulations at the top of the atmosphere (TOA) and at the surface (SFC) with a comparison against the satellite-derived 11 yr (2000–2010) mean CERES_EBAF datasets (http://ceres.larc.nasa.gov/order_data.php). We focus on the results of OLD, NEW_MRO_OL, and NEW_MRO in this section.

The central panels of Fig. 1 show that the new scheme (NEW_MRO_OL and NEW_MRO cases) obtains much improved net all-sky LW and SW TOA radiative fluxes. This is due to both improvement in the revised cloud optics and net clear-sky fluxes calculated by the new radiation scheme in this work.

Compared with CERES_EBAF data, the OLD run shows notable discrepancies in TOA LW and SW CRF (right panels of Fig. 1), which are overestimated by $\sim 3\,\mathrm{Wm^{-2}}$ and $\sim 7\,\mathrm{Wm^{-2}}$, respectively. The offline NEW_MRO_OL run shows large reductions in

these biases (except for LW CRF at the surface), with TOA LW and SW CRF errors reduced to ~ 0.5 and $\sim 1.5\,\mathrm{Wm^{-2}}$, respectively. The interactive NEW_MRO run mostly retains the features of NEW_MRO_OL. As the same cloud overlap assumptions are used, the improved CRF in NEW_MRO and NEW_MRO_OL runs should come mainly from the revised cloud optics (see Table 1). Moreover, the differences in CRF between NEW_MRO and NEW_MRO_OL are also distinct, indicating that clouds have changed noticeably compared to OLD as a result of introducing the new configuration, which will be discussed below.

As for the clear-sky net flux at TOA (F^{clr}, the left panels in Fig. 1), the OLD run overestimates LW and SW F^{clr} by ~ 5 and $\sim 1.5\,\mathrm{Wm^{-2}}$, respectively. The biases at the surface are also large, up to $\sim 4\,\mathrm{Wm^{-2}}$ for SW F^{clr}. Again, NEW_MRO_OL and NEW_MRO produce clear-sky fluxes much closer to the observations (except for LW F^{clr} at surface). The differences between the simulated TOA LW F^{clr} and SW F^{clr} and those from CERES_EBAF observation are reduced to ~ 2 and $\sim 0.5\,\mathrm{Wm^{-2}}$, respectively, for both NEW_MRO_OL and NEW_MRO.

The improvements in both F^{clr} and CRF suggest that the implementation of the McICA with our new radiation scheme fares much better at modeling the inner balance between the radiation components from clear and cloudy regimes. Thus, the new configuration behaves in a more physically coherent manner than the original one in our BCC_AGCM2.0.1, and it predictably yields more reasonable all-sky net fluxes (F^{net}, central panels of Fig. 1).

The other results shown in Fig. 1 will be explained in Sects. 4.2.1 and 4.3.1.

Figure 2 displays zonal annual mean F^{clr}, F^{net}, and CRF at the TOA from the OLD, NEW_MRO_OL, and NEW_MRO runs, as well as the CERES_EBAF dataset. The simulated zonal distributions of these variables are all in reasonable agreement with observations. However, the NEW_MRO and NEW_MRO_OL runs give LW and SW F^{net} much closer to observations, especially at mid–low latitudes (Fig. 2c, d). This occurs mainly because the vast overestimation of LW and SW CRF by the OLD scheme is reduced overall by the new scheme (Fig. 2e, f). Moreover, NEW_MRO and

NEW_MRO_OL also show notable improvement in LW F^{clr} in the subtropics and mid-latitudes (Fig. 2a). The SW F^{clr} is calculated well at most latitudes in all experiments, except at the Polar Regions where there are noticeable underestimations. This may be linked to the enhanced solar albedo over snow surfaces compared with observations in the Community Land Model version 3 (CLM3) used in the BCC_AGCM2.0.1 model (Oleson et al., 2003), which results in overestimated solar energy loss to space.

We will provide detailed discussions of the simulated TOA CRF here and in the following two paragraphs. Figures 3 and 4 show the global distribution of errors in annual mean LW and SW CRF relative to CERES_EBAF, as well as the differences between NEW_MRO_OL and OLD. In the OLD run, LW CRF is overestimated over most tropical and subtropical oceans with very few exceptions, but it is underestimated over intensively convective tropical regions such as central Africa, the west Pacific warm pool, and the Amazon forests of South America (Fig. 3a). The NEW_MRO and NEW_MRO_OL produced similar distributions of these biases; however, the positive biases in tropical and subtropical oceans are reduced, whereas the negative biases are enhanced somewhat (Fig. 3b, c). Figure 3d shows that the initial differences in LW CRF between the new and old configurations are located mainly in the intertropical convective zone (ITCZ) and in high altitude areas such as the Tibetan Plateau and Andes Mountains, with maximum values of more than $6\,\mathrm{W\,m^{-2}}$. As these areas are all sufficient in high-level ice clouds, the differences may be ascribed to the different ice-cloud optical properties used in the two configurations.

The OLD run exhibits negative biases in SW CRF at most low and mid-latitudes (see Fig. 4a). Again, the NEW_MRO_OL and NEW_MRO runs significantly reduce these errors (see Fig. 4b, c), but enhanced positive biases appear over subtropical oceans near the west coasts of continents and over East Asia. Interestingly, the initial differences in SW CRF between the new and old configurations (see Fig. 4d) show a quite similar geographic distribution to those of LW CRF (see Fig. 3d), with a maximum value of more than $14\,\mathrm{W\,m^{-2}}$ in the tropical East Pacific. There are only minor differences in areas with large SW CRF along 60° S, where a large amount of low-level cloud (mostly

Title Page

Abstract | Introduction

Conclusions | References

Tables | Figures

|◀ | ▶|

◀ | ▶

Back | Close

Full Screen / Esc

Printer-friendly Version

Interactive Discussion

liquid) exists (see Fig. 2f), because the liquid cloud optics in the two configurations are almost equivalent for CRF calculation. Consequently, the changes in ice cloud optical properties are the main cause of the changed SW and LW CRF in the McICA runs.

The cooling effect by SW CRF and heating effect by LW CRF at the TOA in tropical deep convective regions have been shown to be nearly linearly correlated and to generally compensate for each other (Kiehl and Ramanathan, 1990), which means that the (SW CRF)/(LW CRF) slope is about −1. This slope is often used as a criterion for showing the performance of modeled CRF. The (SW CRF)/ (LW CRF) slopes in the Indonesian region (10° S–20° N, 110–160° E) for various simulations and CERES_EBAF observations are given in Table 2. The table shows that the OLD run overestimates the (SW CRF)/(LW CRF) slopes for the annual mean and for different seasons. NEW_MRO shows a generally noticeable decrease in SW CRF, especially for the annual mean and summer (JJA). This results in decreased (SW CRF)/(LW CRF) slopes (Table 2). As shown in Table 2, NEW_MRO_OL gives very similar results to OLD. Thus, it can be inferred that the two model configurations are comparable for diagnosing the SW and LW CRF ratio, whereas the climate feedback evidently changes the simulated cloud fractions. This will be addressed later.

Radiative heating/cooling within the atmosphere is a critical driving factor in climate simulation. Figures 5 and 6 compare the clear-sky and all-sky LW heating rate of NEW_MRO_OL and OLD, respectively. For the clear-sky condition, NEW_MRO_OL shows a remarkable (more than 10 %) cooling trend in the lower troposphere within 60° S–60° N and a heating trend in most of the middle troposphere. These may be related to the different treatments of greenhouse gases, especially O_3 and water vapor. The difference in the all-sky LW heating rate (see Fig. 6c) is similar to the pattern shown in Fig. 5c, indicating that differences in the heating rates of clouds are less important for determining the final state in this case. This pattern tends to increase the stability of the atmosphere below 600 hPa but enhance vertical mixing above 600 hPa. The differences in SW heating rate are much smaller than are those for LW (figure not shown).

Application and evaluation of McICA scheme

H. Zhang et al.

Title Page

Abstract | Introduction

Conclusions | References

Tables | Figures

|◄ | ►|

◄ | ►

Back | Close

Full Screen / Esc

Printer-friendly Version

Interactive Discussion

As shown above, the application of the McICA scheme with BCC-RAD remarkably influences the radiation budget at both boundaries and within the atmosphere. These changes will extensively affect the final simulated climate.

4.1.2 Surface climatology

In this subsection, the simulated surface temperature and precipitation in two seasons (DJF and JJA) are evaluated.

Zonal comparisons of surface temperature are shown in Fig. 7. Although both NEW_MRO and OLD yield similar zonal mean distributions compared with the ERA-40 reanalysis data, there are substantial differences between both simulations and the ERA-40 (Uppala et al., 2005). For instance, in DJF, surface temperatures are underestimated by about 1.5 K in the mid-latitudes and by 6–7 K around the North Pole (see Fig. 7a); in JJA, the zonal mean negative biases reach a maximum of 3–4 K at 60–70° S/N (see Fig. 7b). The global distribution of surface temperature biases from the NEW_MRO and OLD runs are quite similar (figures not shown), with local maximum differences between the NEW_MRO and OLD runs reaching ±2–4 K. The differences between the simulations and observation are much larger than the differences between the NEW_MRO and OLD simulations.

Similar to Fig. 7, Fig. 8 shows comparisons of the precipitation rate. Both the NEW_MRO and OLD simulations capture the main features of the meridional distribution of precipitation, such as the maximum in the Tropics and secondary maxima at the mid-latitude storm tracks. However, errors are also clear relative to observations, especially in the Tropics (gray lines in Fig. 8a, b). The two simulations are comparable in their simulation of the zonal mean distribution of precipitation, but there are noticeable local differences in the tropical and subtropical regions (figures not shown). These differences probably result from the altered atmospheric thermodynamics and dynamics caused by changes in the radiation budget. The increases and decreases in precipitation often coincide with the decreases and increases in surface temperature

(figures not shown), respectively; thus, the changes in precipitation obviously influence the surface energy balance.

It should be noted that, in this work, we altered only the sub-grid cloud structures used in the radiation calculation, whereas those in precipitation parameterization were not changed. Physically, cloud overlaps in the radiation and precipitation processes should be consistent with each other, but the latter may have a larger effect on the simulated precipitation (Morcrette and Jakob, 2000). However, this is beyond the scope of this study.

4.1.3   Atmospheric states

Simulated atmospheric temperature, specific humidity, and cloud condensation (water and ice) are analyzed in this subsection.

Figure 9 shows comparisons of the latitude–height distribution of atmospheric temperature. Notable cold biases relative to ERA-40, about 1–2 degrees in the low–mid troposphere, exist throughout almost the entire troposphere in the OLD case (see Fig. 9a). The NEW_MRO simulation inherits most of these biases, but the relative warming (up to 0.4–0.8 K) within the central troposphere (800 ∼ 500 hPa) is a desirable change compared with OLD (see Fig. 9c). This is definitely related to the reduced LW cooling rate in the central troposphere, as shown in Figs. 5 and 6.

Likewise, Fig. 10 shows comparisons of atmospheric specific humidity. In addition to the improvements in tropospheric temperature, there are favorable changes in specific humidity. Compared with ERA-40, the OLD run is subject to considerable dry biases in the tropical lower troposphere (see Fig. 10a). This is likely caused by LW heating rate biases related to the LW parameterization of water vapor (Collins et al., 2002). Due to changes in heating rate, as shown in Figs. 5 and 6, the NEW_MRO run notably increases the specific humidity in the Tropics, typically reducing the original biases by about 30 %.

The changes in atmospheric temperature and specific humidity exert influences on the formation and maintenance of cloud water and ice (figures not shown), affecting

the modeled local radiation budget, such as by altering the SW and LW CRF ratios, as mentioned above.

Overall, the incorporation of the new scheme influences radiative fluxes and heating rates remarkably. Due to these changes, the simulated surface and atmospheric climate are comparable or improved relative to the old model configuration. Therefore, the new scheme used here has been demonstrated to be a viable option for long-term climate simulation.

It should also be mentioned that the differences in simulated climate between the two model configurations are relatively smaller than are those between the simulations and observations. Nevertheless, the much more flexible cloud structure and internal consistency of the new configuration will benefit further development of model physics. In regard to the convenience of the McICA scheme for modifying sub-grid clouds, the impact of the cloud structure variations is assessed as follows.

4.2 The impact of altering the cloud overlap assumption

Tests NEW_GO1, NEW_GO2, and NEW_GO3 implemented GenO with L_{cf} set at 1, 2, and 3 km, respectively. In GenO, the overlap of two vertical cloud layers depends on L_{cf}. For two fixed cloud layers, the larger L_{cf} is, the more they tend toward maximum overlap; conversely, smaller L_{cf} results in a tendency toward random overlap (Eqs. 4–7). The sensitivity of the simulations to changes in cloud overlap assumptions is demonstrated by the differences among the NEW_GO1, NEW_GO2, NEW_GO3, and NEW_MRO tests.

4.2.1 Radiation and cloud fraction

The 2nd to 6th columns in each panel of Fig. 1 show the global annual mean radiation budget from McICA runs with different cloud vertical overlap assumptions. As expected, both LW and SW CRF decrease from NEW_GO1 to NEW_GO3 because clouds tend increasingly to maximum overlap, and cloud fractions decrease. As also seen in Fig. 1,

NEW_MRO shows the smallest CRF among the McICA runs with the PPH assumption. This occurs because BCC_AGCM2.0.1 tends to generate frequent occurrences of vertically continuous cloudy layers. Thus NEW_MRO, which depends on the separation of cloudy layers to arrange the cloud vertical distribution, tends to underestimate the verti-
5 cally projected cloud fraction and diminish CRF. This has also been proven in previous studies using the CAM3 model (Barker and Räisänen, 2005). Quantitatively, the extent of variations in global mean CRF caused by changes in cloud overlap is here about 1 Wm^{-2} for LW and 2 Wm^{-2} for SW (at both the TOA and surface). However, CRF is more accurately represented in all the McICA simulations than in the OLD run.
10   As all the McICA tests considered in this section adopt the PPH assumption and the same cloud optical properties, the differences in the modeled radiation fields stem predominantly from differences in the vertically projected cloud fraction. Figure 11 compares the annual mean total cloud fraction (C_{TOT}) from all the simulations with ISCCP observations. Although the NEW_MRO run roughly captures the meridional variation in
15 C_{TOT} (see Fig. 11a, b), Fig. 11c shows that it generally overestimates (underestimates) total cloud fraction in the Tropics and at high latitudes (in the mid-latitudes), typically by 20–30 %. When using GenO with L_{cf} = 1 km, the positive (negative) biases in the Tropics and high latitudes (mid-latitudes) are enlarged (shrunken) (see Fig. 11d). When L_{cf} is increased to 3 km (Fig. 11f), the positive biases decrease in the Tropics and at
20 higher latitudes, whereas the negative biases in the mid-latitudes increase compared with NEW_GO1. This indicates that a larger L_{cf} should be used in tropical regions and at high latitudes and a smaller L_{cf} should be used in mid-latitude areas to make the modeled total cloud fraction more realistic.

     Note that even 3 km of L_{cf} is not yet enough in the Tropics. A considerable portion
25 of clouds, especially the deep convective type, possesses a larger L_{cf} of even more than 10 km in some cases (Barker, 2008), so there is still space left in which to constrain the presentation of cloud overlap. Additionally, the cloud overlap procedure is done on cloud profiles provided by the diagnostic cloud fraction scheme based on only

relative humidity (Rasch and Kristjansson, 1998), and cloud fraction also can be more accurately calculated by its improvement.

The zonal mean biases in modeled C_{TOT} are shown in Fig. 12a. As stated above, all simulations generate larger (smaller) C_{TOT} than observation in the Tropics and at high latitudes (mid-latitudes); the positive biases in the Tropics and at high latitudes decrease as the L_{cf} used in GenO increases (and vice versa for the mid-latitudes). Also shown in Fig. 12b–d are the differences in modeled low ($> 700\,\text{hPa}$), middle (700–400 hPa), and high ($< 400\,\text{hPa}$) cloud fractions between other McICA runs and NEW_MRO. The maximum differences between NEW_GO1 and NEW_MRO are up to 5–7 % in the Tropics for all cloud levels, and those between NEW_GO3 and NEW_MRO reach 2–3 %. Although the differences generally decrease poleward for low and middle clouds, the modeled high clouds differ as much at high latitudes as in the Tropics. This occurs because at high latitudes, modeled lower-level clouds are more frequently overcast or near overcast, whereas higher-level clouds are much less likely to occupy a grid cell (figure not shown). These remarkable differences in cloud fractions at different levels exert large influences on modeled CRFs.

Figures 13 and 14 show the differences in LW and SW CRF, respectively, during DJF and JJA. NEW_GO1 primarily blocks more LW flux emitted upward (see Fig. 13a, d) and reflects more SW flux (see Fig. 14a, d) than NEW_MRO does due to the increased cloud fraction. The greatest differences tend to appear in the tropical region and around the 60° S/N storm tracks, especially over the ITCZ and SPCZ regions, with local maximums of more than $10\,\text{W}\,\text{m}^{-2}$ for LW CRF and more than $20\,\text{W}\,\text{m}^{-2}$ for SW CRF. This pattern occurs because clouds in these regions are often vertically extensive and thus the overlap assumption plays a more critical role in judging the vertically integrated cloud fraction. Figure 14 shows that from NEW_GO1 to NEW_GO3, SW CRF increases remarkably in the Tropics and storm track regions. Considering the basically negative biases of SW CRF in these regions (see Fig. 4), this implies that SW CRF may be better represented in these regions by increasing L_{cf}.

4.2.2 Simulated climate

Figures 15 and 16 show the zonal annual mean biases in surface temperature and precipitation of various McICA runs with different vertical cloud structures. All simulations yield almost identical surface temperatures at low latitudes (see Fig. 15a, b). However, there are clear discrepancies at the mid–high latitudes, especially during DJF in the Northern Hemisphere, where the largest difference reaches almost 1 K (NEW_GO1NEW_MRO). This may be attributed to the enhanced LW warming effect below cloud base in NEW_GO1 due to the increased cloud fraction. Although a SW cooling effect is also seen in NEW_GO1 because of increased reflection at cloud top, the LW warming effect seems dominant during DJF in the Northern Hemisphere. It is worth addressing the fact that the ranges of temperature variation in the mid–high latitudes caused by changing the overlap assumption may surpass the differences between the two model configurations in this work (see Fig. 7).

Surface precipitation (see Fig. 16a, b), atmospheric temperature, and humidity were also examined in NEW_GO1–NEW_GO3 (figure not shown), and we obtained similar results to those for NEW_MRO. So, the changes in the cloud overlap assumption are not likely to cause a direct, notable shift in simulated atmospheric states, etc., although the impacts of overlap assumptions on heating rates have been emphasized in offline diagnostics (see Barker et al., 1999; Li et al., 2005). It should be noted that sea–atmosphere interaction is not considered here and that it might strengthen the signal imposed on the climate system by changing the cloud overlap assumption.

4.3 The impact of breaking the PPH assumption

In this subsection, we briefly consider the impacts of breaking the traditional PPH assumption on simulated radiation and climate by comparing the NEW_GO2_IH and NEW_GO2 tests.

4.3.1 Radiation

From a global mean perspective, the changes in CRF and net fluxes caused by including horizontally inhomogeneous cloud condensation (Eq. 8) are as large as or even larger than the changes from altering the cloud overlap assumptions (see NEW_GO2_IH in Fig. 1), which has also been shown by calculations from cloud-resolving models (Barker and Räisänen 2005). The global mean reductions in LW CRF and SW CRF at the TOA are about 1.2 and 3.7 W m^{-2}, respectively. The consideration of horizontally inhomogeneous clouds brings the global mean CRF and F^{net} much closer to observations.

Figure 17 shows the differences in LW CRF and SW CRF between NEW_GO2_IH and NEW_GO2 for DJF and JJA. It can be seen that NEW_GO2_IH mainly decreases LW and SW CRF all over the globe, with local maximum reductions of more than 10 and 20 W m^{-2}, respectively, in the Tropics (especially the warm pool) and secondary reductions in the mid-latitudes. This is qualitatively consistent with the well-accepted conclusion that the PPH assumption of cloud condensation generally overestimates solar reflectance (Carlin et al., 2002) and LW emissivity (Pomroy and Illingworth, 2000) due to the nonlinear dependence of radiative effects on cloud water content. These changes can somewhat offset the positive (negative) differences in LW (SW) CRF in the PPH runs (see Figs. 3 and 4). Thus, it is of great importance to address the cloud water/ice horizontal distribution together with the overlap of fractional clouds in GCMs.

4.3.2 Simulated climate

The consideration of cloud horizontal distribution has a noticeable influence on surface temperature (see NEW_GO2_IH in Fig. 15). In the mid–high latitudes of the Northern Hemisphere, there is a remarkable decrease in surface temperature during DJF and an increase during JJA. These changes arise mainly from competition between LW cooling and SW heating. When inhomogeneous clouds succeed homogeneous ones, more LW flux is emitted outward, and more SW flux penetrates to the surface (see

Fig. 1). The surface energy budget is then a result of the competition between the two fluxes.

For other climate elements, such as precipitation, air temperature, specific humidity, surface pressure, zonal winds, and so forth (figures not shown), the differences between NEW_GO2_IH and NEW_GO2 are minor, like those between different overlap assumptions.

Generally speaking, modifications of cloud sub-grid configurations have distinct impacts on the simulated radiation budget and surface temperature. Considering the improved LW and SW budget for clear-sky and all-sky conditions, the new model configuration can be used in BCC_AGCM2.0.1 to improve physical processes and perform climate simulations.

5 Discussion and conclusions

The McICA scheme with the BCC-RAD radiation code was incorporated into the BCC_AGCM2.0.1 model in this work as a replacement for the original CAM3 cloud-radiation scheme. This new configuration is flexible for treating arbitrarily complex sub-grid cloud structures, including the vertical overlap of fractional clouds and horizontal distribution of cloud condensation. The advantages of the new configuration suggest that it is a better option for future development of BCC_AGCM2.0.1. This work aimed to investigate the impact of this modification on climate simulated by BCC_AGCM2.0.1. Several configurations of sub-grid cloud structures, including variations in vertical overlap and horizontal distribution, were tested, and the model's sensitivity to changes in cloud structures and the newly adopted radiation scheme were exhibited and clarified.

The results show that the new scheme markedly improves the representation of the SW and LW radiation budget for both clear-sky and all-sky conditions, whether in the global mean or in geographic distribution. The simulated relationship between SW and LW CRFs in deep convective regions is improved by the new scheme compared with the old scheme. These results all indicate that using the McICA scheme with

our BCC-RAD code makes the cloud-radiation process more intrinsically coherent and reasonable. The modeled temperature and specific humidity benefited from changes in the LW heating rate, resulting in a reduction in temperature biases by 0.4–0.8 $^\circ$C at the middle troposphere and a reduction in moisture biases by 1/3 in the tropical lower troposphere relative to the ERA-40 reanalysis. This shows the superior of a CKD radiation algorithm to the band model based CAM3 radiation scheme.

The impacts of altering cloud overlap within the McICA scheme were assessed by including a so-called "general overlap." Results demonstrated that changes in cloud overlap assumptions have remarkable effects on the boundary radiation budgets. The global annual mean SW (LW) CRF differs by at most $\sim 2\,\mathrm{Wm}^{-2}$ ($\sim 1\,\mathrm{Wm}^{-2}$) at both the TOA and surface, with the test NEW_GO1 (L_cf = 1 km) always showing the largest CRF and the test NEW_MRO always showing the smallest due to differences in cloud cover generation. CRF in the Tropics and storm track regions, especially over the ITCZ and the SPCZ, is most notably influenced by the choice of overlap assumptions due to frequently occurring extensive clouds, with local differences of $> 10\,\mathrm{Wm}^{-2}$ for LW CRF and $> 20\,\mathrm{Wm}^{-2}$ for SW CRF. It is found in this work that the results of cloud fraction and CRF are very sensitive to the chosen of L_cf, especially in the Tropics and mid-latitude storm track regions. Therefore a constant value of L_cf can always lead large bias in climate simulations.

The effect of horizontal inhomogeneity of cloud condensation was then considered by including an observation-based gamma function in an additional test. The changes compared with its PPH counterpart test were strikingly significant, with decreases in global mean TOA longwave and shortwave CRF of $\sim 1.2\,\mathrm{Wm}^{-2}$ and $\sim 3.7\,\mathrm{Wm}^{-2}$, respectively, making the simulation results much closer to the observations. This emphasizes the importance of addressing cloud horizontal distribution in GCMs along with the cloud overlap issue. However, the cloud horizontal inhomogeneity has not been paid enough attention in climate simulations so far.

For simulated climate, the changes in cloud structures showed a notable effect on surface temperatures in mid–high latitudes, with the largest zonal mean differences

being about 1 K, exceeding the differences between the new and old configurations. The impacts on precipitation and atmospheric temperature were minor. However, it should be noted that we did not here include sea–atmosphere interaction, which could enlarge the effect of the signal imposed by the changing cloud structures.

The results of this study are encouraging for future improvement of the McICA. By analyzing the CloudSat dataset, Zhang et al. (2013b) have found that the decorrelation depth is usually changeable from 0–3 km or more depending on area and season, except for individual areas with values larger than 9 km. However, the current McICA scheme usually adopts the decorrelation depth of a constant 2 km over the globe. Because of the substantial flexibility of the McICA scheme, a more realistic cloud overlap assumption or cloud horizontal distribution, achieved from satellite observations or any other objective sources, could be used to constrain the model simulation. Therefore, to make full use of the new scheme, we will consider, as our next work, ways to obtain changeable and reasonable information on global decorrelation depths and implement these into GCMs.

References

Baum, B. A., Heymsfield, A. J., Yang, P., and Bedka, S. T.: Bulk Scattering Properties for the Remote Sensing of Ice Clouds, Part I: Microphysical Data and Models, J. Appl. Meteorol., 44, 1885–1895, 2005.

Barker, H. W.: Overlap of fractional cloud for radiation calculations in GCMs: A global analysis using CloudSat and CALIPSO data, J. Geophys. Res., 113, D00A01, doi:10.1029/2007JD009677, 2008.

Barker, H. W. and Räisänen, P.: Radiative sensitivities for cloud structural properties that are unresolved by conventional GCMs, Q. J. Royal Meteorol. Soc., 131, 3103–3122, 2005.

Barker, H. W., Stephens, G. L., and Fu, Q.: The sensitivity of domain-averaged solar fluxes to assumptions about cloud geometry, Q .J. Royal Meteorol. Soc., 125, 2127–2152, 1999.

Barker, H. W., Cole, J. N. S., Morcrette, J. J., Pincus, R., Räisänen, P., von Salzen, K., and Vaillancourt, P. A.: The Monte Carlo independent column approximation: an assessment using several global atmospheric models, Q. J. Royal Meteorol. Soc., 134, 1463–1478, 2008.

Briegleb, B. P.: Delta-Eddington approximation for solar radiation in the NCAR Community Climate Model, J. Geophys. Res., 97, 7603–7612, 1992.

Cahalan, R. F., Ridgway, W., Wiscombe, W. J., Gollmer, S., and Harshvardhan, Independent Pixel and Monte Carlo Estimates of Stratocumulus Albedo, J. Atmos. Sci., 51, 3776–3790, 1994.

Carlin, B., Fu, Q., Lohmann, U., Mace, G. G., Sassen, K., and Comstock, J. M.: High-Cloud Horizontal Inhomogeneity and Solar Albedo Bias, J. Clim., 15, 2321–2339, 2002.

Clough, S. A. and Iacono, M. J.: Line-by-line calculation of atmospheric fluxes and cooling rates 2: Application to carbon dioxide, ozone, methane, nitrous oxide and the halocarbons, J. Geophys. Res., 100, 16519–16535, 1995.

Coakley, J. A., Cess, R. D., and Yurevich, F. B.: The Effect of Tropospheric Aerosols on the Earth'sRadiation Budget: A Parameterization for Climate Models, J. Atmos. Sci., 40, 116–138, 1983.

Collins, W. D.: Parameterization of Generalized Cloud Overlap for Radiative Calculations in General Circulation Models, J. Atmos. Sci., 58, 3224–3242, 2001.

Collins, W. D., Hackney, J. K., and Edwards, D. P.: An updated parameterization for infrared emission and absorption by water vapor in the National Center for Atmospheric Research Community Atmosphere Model, J. Geophys. Res., 107, doi:10.1029/2001JD001365, 2002.

Ebert, E. E. and Curry, J. A.: A Parameterization of Ice Cloud Optical Properties for Climate Models, J. Geophys. Res, 97, 3831–3836, 1992.

Ellingson, R. G., Ellis, J., and Fels, S.: The Intercomparison of Radiation Codes Used in Climate Models: Long Wave Results, J. Geophys. Res., 96, 8929–8953, 1991.

Fu, Q.: An Accurate Parameterization of the solar radiative properties of cirrus clouds for climate models, J. Clim., 9, 2058–2082, 1996.

Fu, Q. and Liou, K. N.: On the Correlated k-Distribution Method for Radiative Transfer in Non-homogenecous Atmospheres, J. Atmos. Sci., 49, 2139–2156, 1992.

Application and evaluation of McICA scheme

H. Zhang et al.

Title Page

Abstract | Introduction

Conclusions | References

Tables | Figures

◀ | ▶

◀ | ▶

Back | Close

Full Screen / Esc

Printer-friendly Version

Interactive Discussion

Gong, S. L., Barrie, L. A., Blanchet, J. P., von Salzen, K., Lohmann, U., Lesins, G., Spacek, L., Zhang, L. M., Girard, E., Lin, H., Leaitch, R., Leighton, H., Chylek, P., and Huang, P.: Canadian Aerosol Module: A size-segregated simulation of atmospheric aerosol processes for climate and air quality models 1. Module development, J. Geophys. Res., 108, 864007, doi:10.1029/2001JD002002, 2003.

Hong, G., Yang, P., Baum, B. A., Heymsfield, A. J., and Xu, K. M.: Parameterization of Short-wave and Longwave Radiative Properties of Ice Clouds for Use in Climate Models, J. Clim., 22, 6287–6312, 2009.

IPCC: Climate Change 2007: Impacts, Adaptation and Vulnerability. Contribution of Working Group II to the Fourth Assessment Report of the Intergovernmental Panel on Climate Change, Cambridge University Press, Cambridge, 2007.

Jing, X. W. and Zhang, H.: Application and evaluation of McICA scheme in BCC_AGCM2.0.1, AIP Conf. Proc., 1531, 756–759, doi:10.1063/1.4804880, 2013.

Kiehl, J. T. and Briegleb, B. P.: A new parameterization of the absorptance due to the 15 μm band system of carbon dioxide, J. Geophys. Res., 96, 9013–9019, 1991

Kiehl, J. T. and Ramanathan, V.: Comparison of Cloud Forcing Derived From the Earth Radiation Budget Experiment with That Simulated by the NCAR Community Climate Model, J. Geophys. Res., 95, 11679–11698, 1990.

Kiehl, J. T., Hack, J. J., and Briegleb, B. P.: The simulated Earth radiation budget of the National Center for Atmospheric Research Community Climate Model CCM2 and comparisons with the Earth Radiation Budget Experiment (ERBE), J. Geophys. Res., 99, 20815–20827, 1994.

Kratz, D. P.: The correlated k-distribution technique as applied to the AVHRR channels, J. Quantitative Spectrosc. Radiat. Transf., 53, 501–517, 1995.

Kristjansson, J. E., Edwards, J. M., and MitChell, D. L.: Impact of a new scheme for optical properties of ice crystals on climates of two GCMs, J. Geophys. Res., 105, 10063–10079, 2000.

Li, J., Dobbie, S., Räisänen, P., and Min, Q.: Accounting for unresolved clouds in a 1-D solar radiative-transfer model, Q. J. Royal Meteorol. Soc., 131, 1607–1629, 2005.

Liang, X. Z. and Wu, X.: Evaluation of a GCM subgrid cloud-radiation interaction parameterization using cloud-resolving model simulations, Geophys. Res. Lett., 32, L06801, doi:10.1029/2001JD002002, 2005.

Lu, P., Zhang, H. and Jing, X. W.: The effects of different HITRAN versions on calculated longwave radiation and uncertainty evaluation, Acta Meteor. Sinica, 26, 389–398, 2012.

Application and evaluation of McICA scheme

H. Zhang et al.

Mace, G. G. and Benson-Troth, S.: Cloud-Layer Overlap Characteristics Derived from Long-Term Cloud Radar Data, J. Clim., 15, 2505–2515, 2002.

Morcrette, J. J. and Jakob, C.: The Response of the ECMWF Model to Changes in the Cloud Overlap Assumption, Mon. Weather Rev., 128, 1707–1732, 2000.

Morcrette, J. J., Barker, H. W., Cole, J. S., Iacono, M. J., and Pincus, R.: Impact of a new radiation package, McRad, in the ECMWF Integrated Forecasting System, Mon. Weather Rev., 136, 4773–4798, doi:10.1175/2008MWR2363.1, 2008.

Nakajima, T., Tsukamoto, M., Tsushima, Y., Numaguti, A., and Kimura, T.: Modeling of the Radiative Process in an Atmospheric General Circulation Model, Appl. Opt., 39, 4869–4878, 2000.

Naud, C. M., Del Genio, A., Mace, Gerald G., Benson, S., Clothiaux, E. E., and Kollias, P.: Impact of Dynamics and Atmospheric State on Cloud Vertical Overlap, J. Clim., 21, 1758–1770, 2008.

Neale, R. B., Chen, C. C., Andrew, G., Lauritzen, P. H., Park, S., Williamson, D. L., Conley, A. J., Garcia, R., Kinnison, D., Lamarque, J. F., Marsh, D., Mills, M., Smith, A. K., Tilmes, S., Vitt, F., Morrrison, H., Cameron-Smith, P., Collins, W. D., Iacono, M. J., Easter, R. C., Ghan, S. J., Liu, X., Rasch, P. J., and Taylor, M. A.: Description of the NCAR Community Atmosphere Model (CAM 5.0). NCAR Tech. Note TN-486, available at: http://www.cesm.ucar.edu/models/cesm1.2/cam/docs/description/cam5_desc.pdf, 2010.

Oleson, K. W., Bonan, G. B., Schaaf, C., Gao, F., Jin, Y., and Strahler, A.: Assessment of global climate model land surface albedo using MODIS data, Geophys. Res. Lett., 30, 1443, doi:10.10292002GL016749, 2003.

Oreopoulos, L. and Davies, R.: Plane Parallel Albedo Biases from Satellite Observations. Part I: Dependence on Resolution and Other Factors, J. Clim., 11, 919–932, 1998.

Pincus, R., Barker, H. W., and Morcrette, J. J.: A fast, flexible, approximate technique for computing radiative transfer in inhomogeneous cloud fields, J. Geophys. Res., 108, 4376, doi:10.1029/2002JD003322, 2003.

Pomroy, H. R. and Illingworth, A. J.: Ice cloud inhomogeneity: Quantifying bias in emissivity from radar observations, Geophys. Res. Lett., 27, 2101–2104, 2000.

Räisänen, P. and Barker, H. W.: Evaluation and optimization of sampling errors for the Monte Carlo Independent Column Approximation, Q. J. Royal Meteorol. Soc., 130, 2069–2085, 2004.

Räisänen, P. and Järvinen, H.: Impact of cloud and radiation scheme modifications on climate simulated by the ECHAM5 atmospheric GCM, Q. J. Royal. Meteorol. Soc., 136, 1733–1752, 2010.

Räisänen, P., Barker, H. W., Khairoutdinov, M. F., Li, J., and Randall, D. A.: Stochastic generation of subgrid-scale cloudy columns for large-scale models, Q. J. Royal Meteorol. Soc., 130, 2047–2067, 2004.

Ramanathan, V. and Downey, P.: A nonisothermal emissivity and absorptivity formulation for water vapor, J. Geophys. Res., 91, 8649–8666, 1986.

Randles, C. A., Kinne, Myhre, S., Schulz, M., Stier, P., Fischer, J., Doppler, L., Highwood, E., Ryder, C., Harris, B., Huttunen, J., Ma, Y., Pinker, R. T., Mayer, B., Neubauer, D., Hitzenberger, R., Oreopoulos, L., Lee, D., Pitari, G., Di Genova, G., Quaas, J., Rose, F. G., Kato, S., Rumbold, S. T., Vardavas, I., Hatzianastassiou, N., Matsoukas, C., Yu, H., Zhang, F., Zhang, H., and Lu, P.: Intercomparison of shortwave radiative transfer schemes in global aerosol modeling: results from the AeroCom Radiative Transfer Experiment, Atmos. Chem. Phys., 13, 2347–2379. doi:10.5194/acp-13-2347-2013, 2013.

Rasch, P. J. and Kristjansson, J. E.: A comparison of the CCM3 model climate using diagnosed and predicted condensate parameterizations, J. Clim., 11, 1587–1614, 1998.

Rothman, L. S., Barbe, A. , Chris Benner, D., Brown, L. R., Camy-Peyret, C., Carleer, M. R., Chance, K., Clerbaux, C., Dana, V., Devi, V. M., Fayt, A., Flaud, J. M., Gamache, R. R., Goldman, A., Jacquemart, D., Jucks, K. W., Lafferty, W. J., Mandin, J. Y., Massie, S. T., Nemtchinov, V., Newnham, D. A., Perrin, A., Rinsland, C. P., Schroeder, J., Smith, K. M., Smith, M. A. H., Tang, K., Toth, R. A., Vander Auwera, J., Varanasi, P., and Yoshino, K.: The HITRAN molecular spectroscopic database: edition of 2000 including updates through 2001, J. Quantitative Spectrosc. Radiat. Transf., 82, 5–44, 2003.

Shonk, J. K. P. and Hogan, R. J.: Tripleclouds: An Efficient Method for Representing Horizontal Cloud Inhomogeneity in 1-D Radiation Schemes by Using Three Regions at Each Height, J. Clim., 21, 2352–2370, 2008.

Shonk, J. K. P., Hogan, R. J., Edwards, J. M., and Mace, G. G.: Effect of improving representation of horizontal and vertical cloud structure on the Earth's global radiation budget. Part I: Review and parametrization, Q. J. Royal Meteorol. Soc., 136, 1191–1204, 2010.

Slingo, A.: A GCM Parameterization for the Shortwave Radiative Properties of Water Clouds, J. Atmos. Sci., 46, 1419–1427, 1989.

Title Page

Abstract | Introduction

Conclusions | References

Tables | Figures

◄ | ►

◄ | ►

Back | Close

Full Screen / Esc

Printer-friendly Version

Interactive Discussion

Stephens, G. L., Wood, N. B., and Gabriel, P. M.: An Assessment of the Parameterization of Subgrid-Scale Cloud Effects on Radiative Transfer. Part I: Vertical Overlap, J. Atmos. Sci., 61, 715–732, 2004.

Stubenrauch, C. J., Rossow, W. B., Chéruy, F., Chédin, A., and Scott, N. A.: Clouds as Seen by Satellite Sounders (3I) and Imagers (ISCCP), Part I: Evaluation of Cloud Parameters, J. Clim., 12, 2189–2213, 1999.

Sun, Z. and Rikus, L.: Improved application of ESFT to inhomogeneous atmosphere, J. Geophy. Res., 104, 6291–6303, 1999.

Tian, L. and Curry, J. A.: Cloud Overlap Statistics, J. Geophys. Res., 94, 9925–9935, 1989.

Uppala, S. M., Kållberg, P. W., Simmons, A. J., Andrae, U., Bechtold, V. Da Costa, Fiorino, M., Gibson, J. K., Haseler, J., Hernandez, A., Kelly, G. A., Li, X., Onogi, K., Saarinen, S., Sokka, N., Allan, R. P., Andersson, E., Arpe, K., Balmaseda, M. A., Beljaars, A. C. M., Berg, L. Van De, Bidlot, J., Bormann, N., Caires, S., Chevallier, F., Dethof, A., Dragosavac, M., Fisher, M., Fuentes, M., Hagemann, S., Hólm, E., Hoskins, B. J., Isaksen, L., Janssen, P. A. E. M., Jenne, R., McNally, A. P., Mahfouf, J. F., Morcrette, J. J., Rayner, N. A., Saunders, R. W., Simon, P., Sterl, A., Trenberth, K. E., Untch, A., Vasiljevic, D., Viterbo, P., and Woollen, J.: The ERA-40 re-analysis, Q. J. Royal Meteorol. Soc., 131, 2961–3012, 2005.

Wei, X. D. and Zhang, H.: Analysis of optical properties ofnonspherical dust aerosols, Acta Optica. Sinica, 31, 0501002-1, 2011.

Wu, T. W. and Wu, G. X.: An empirical formula to compute snow cover fraction in GCMs, Adv. Atmos. Sci., 21, 529–535, 2004.

Wu, T., Yu, R., Zhang, F., Wang, Z., Dong, M., Wang, L., Jin, X., Chen, D., and Li, L.: The Beijing Climate Center atmospheric general circulation model: description and its performance for the present-day climate, Clim. Dyn., 34, 123–147, doi:10.1007/s00382-008-0487-2, 2010.

Wyser, K.: The Effective Radius in Ice Clouds, J. Clim., 11, 1793–1802, 1998.

Xie, P. and Arkin, P. A.: Global Precipitation: A 17-Year Monthly Analysis Based on Gauge Observations, Satellite Estimates, and Numerical Model Outputs, Bull. Am. Meteorol. Soc., 78, 2539–2558, 1997.

Yan, H.: The design of a nested fine-mesh model over complex topography part 2: parameterization of sub grid physical processes, Plateau Meteorol, 6, 64–139, 1987(in Chinese).

Yang, P., Wei, H., Huang, H. L., Baum, B. A., Hu, Y. X., Kattawar, G. W., Mishchenko, M. I., and Fu, Q.: Scattering and absorption property database for nonspherical ice particles in the near- through far-infrared spectral region,. Appl. Opt., 44, 5512–5523, 2005.

Title Page

Abstract | Introduction

Conclusions | References

Tables | Figures

◀ | ▶

◀ | ▶

Back | Close

Full Screen / Esc

Printer-friendly Version

Interactive Discussion

Zhang, G. and Mu, M.: Effects of modification to the Zhang-Mcfarlane convection parameterization on the simulation of the tropical precipitation in the National Center for Atmosphere Research Community Climate Model, Version 3, J. Geophys. Res., 110, D09109, doi:10.1029/2004JD00517, 2005.

Zhang, F., Liang, X. Z., Li, J., and Zeng, Q.: Dominant roles of subgrid-scale cloud structures in model diversity of cloud radiative effect, J. Geophys. Res., 118, 7733–7749, doi:10.1002/jgrd.50604, 2013a.

Zhang, H., Nakajima, T., Shi, G., Suzuki, T., and Imasu, R.: An optimal approach to overlapping bands with correlated k-distribution method and its application to radiative calculations, J. Geophys. Res., 108, 4641, doi:10.1029/2002JD003358, 2003.

Zhang, H., Peng, J., Jing, X. W., and Li, J.: The features of clouds overlapping in Eastern Asia and their effect on cloud radiative forcing, Sci. China Earth Sci. ,56, 737–747, 2013b.

Zhang, H., Shi, G., Nakajima, T., and Suzuki, T.: The effect of the choice of the k-interval number on radiative calculation, J. Quant. Spectro. Rad. Trans., 98, 31–43, 2006a.

Zhang, H., Suzuki, T., Nakajima, T., Shi, G., Zhang. X., and Liu, Y.: Effects of band division on radiative calculations, Opt. Eng., 45, 016002, doi:doi:10.1117/1.2160521, 2006b.

Zhang, H., Wang, Z., Wang, Z., Liu, Q., Gong, S., Zhang, X., Shen, Z., Lu, P., Wei, X., Che, H., and Li, L.: Simulation of direct radiative forcing of aerosols and their effects on East Asian climate using an interactive AGCM-aerosol coupled system, Clim. Dyn., 38, 1675–1693, 2012.

Zhou, C. H., Gong, S. L., Zhang, X. Y., Liu, H. L., Xue, M., Cao, G. L., An, X. Q., Che, H. Z., Zhang, Y. M., and Niu, T.: Towards the improvements of simulating the chemical and optical properties of Chinese aerosols using an online coupled model CUACE/Aero, Tellus B, 64, 18965, doi:10.3402/tellusb.v64i0.18965, 2012.

Title Page

Abstract | Introduction

Conclusions | References

Tables | Figures

◀ | ▶

◀ | ▶

Back | Close

Full Screen / Esc

Printer-friendly Version

Interactive Discussion

Table 1. Comparison of the new and old schemes.

	Old	New
Absorbing gases in LW	H_2O, CO_2, and O_3 CH_4, N_2O, CFC11, CFC12	The same as in Old
Absorbing gases in SW	H_2O, CO_2, O_3, and O_2	H_2O, CO_2, O_3, N_2O, and O_2
Range of LW	0–2000 cm^{-1}	0–2680 cm^{-1}
Range of SW	2000–50000 cm^{-1}	2110–49000 cm^{-1*}
Band transmittance scheme	Band model (LW: Kiehl and Briegleb, 1991) (SW: Briegleb, 1992)	CKD scheme Zhang (2003, 2006a, 2006b)
RT solver in LW	Absorptivity/emissivity formulations Ramanathan and Downey (1986)	Two-stream approximation Nakajima et al. (2000)
RT solver in SW	δ–Eddington method Briegleb (1992)	δ–Eddington method Coakley et al. (1983)
Cloud fraction parameterization	Diagnostic scheme Rasch and Kristjansson (1998)	The same as in OLD
Cloud optics	LW: emissivity formulations Ebert and Curry (1992) SW: formulas of Slingo (1989) for liquid and of Ebert and Curry (1992) for ice	Ice cloud: computed using data from Fu (1996), Yang et al. (2005), and Hong et al. (2009) liquid cloud: Nakajima et al. (2000)
Cloud effective radius	Ice cloud: Kristjansson et al. (2000) Liquid cloud: Kiehl et al. (1994)	Ice cloud: Wyser (1998) Liquid cloud: the same as in Old
Cloud overlap	Maximum random overlap (MRO) Collins (2001)	McICA Räisänen and Barker (2004), Barker et al. (2008)
Aerosol-radiation coupling scheme	BCC_AGCM2.0.1_CAM Zhang et al. (2012)	BCC_AGCM2.0.1_CAM Zhang et al. (2012)

* In the new scheme, contributions from the solar spectrum and terrestrial emission are mixed within 2110–2680 cm^{-1}.

Table 2. The modeled and observed (SW CRF)/(LW CRF). slopes in the tropical warm pool region (10° S–20° N, 110° E–160° E).

	OLD	NEW_MRO_OL	NEW_MRO	NEW_GO1	NEW_GO2	NEW_GO3	NEW_GO2_IH	OBS
ANN	−1.17	−1.11	−0.94	−0.94	−1.01	−0.98	−0.98	−1.13
DJF	−1.55	−1.51	−1.34	−1.49	−1.43	−1.41	−1.45	−1.14
JJA	−1.83	−1.65	−1.51	−1.60	−1.57	−1.60	−1.58	−1.09
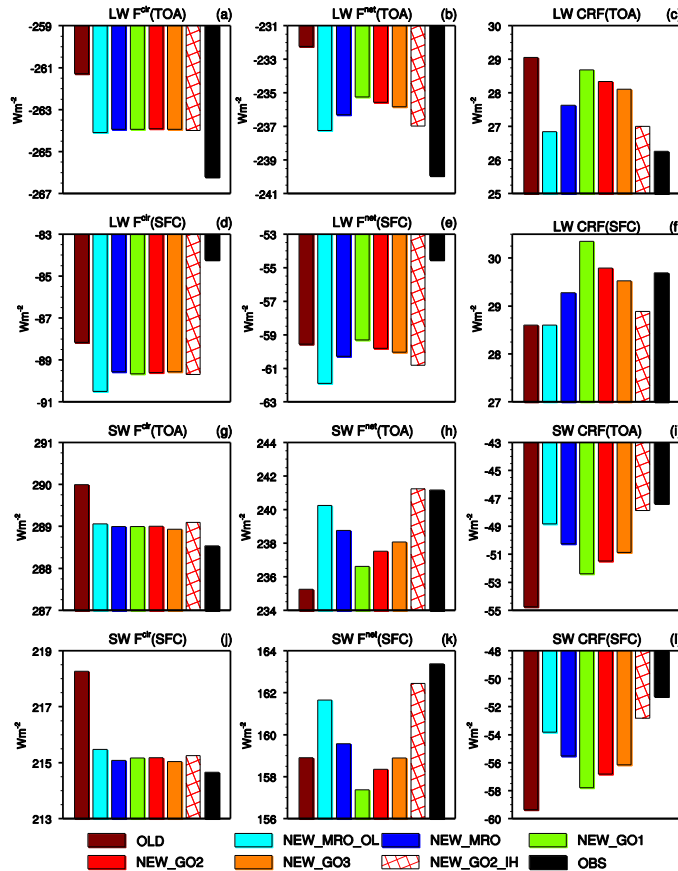
Fig. 1. Global annual mean clear-sky net flux (F^{clr}, left panels), all-sky net flux (F^{net}, central panels), and CRF (right panels) for TOA LW (upmost row), surface LW (second row), TOA SW (third row), and surface SW (bottom row) from the various simulations and CERES_EBAF observations.
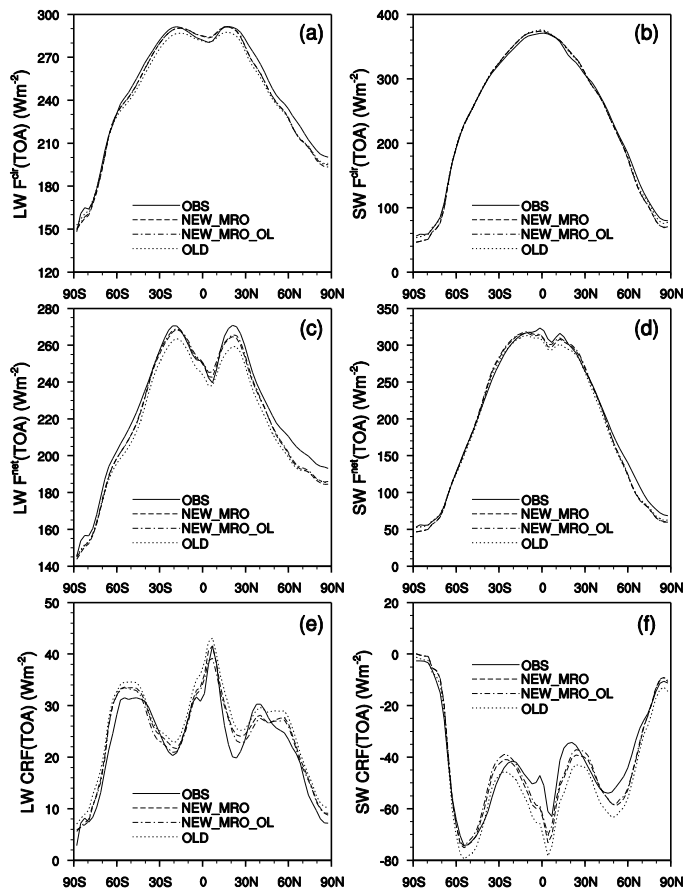
Fig. 2. F^{clr} (top), F^{net} (central), and CRF (bottom) at the TOA for LW (left) and SW (right) from OLD, NEW_MRO, NEW_MRO_OL, and CERES_EBAF observation.
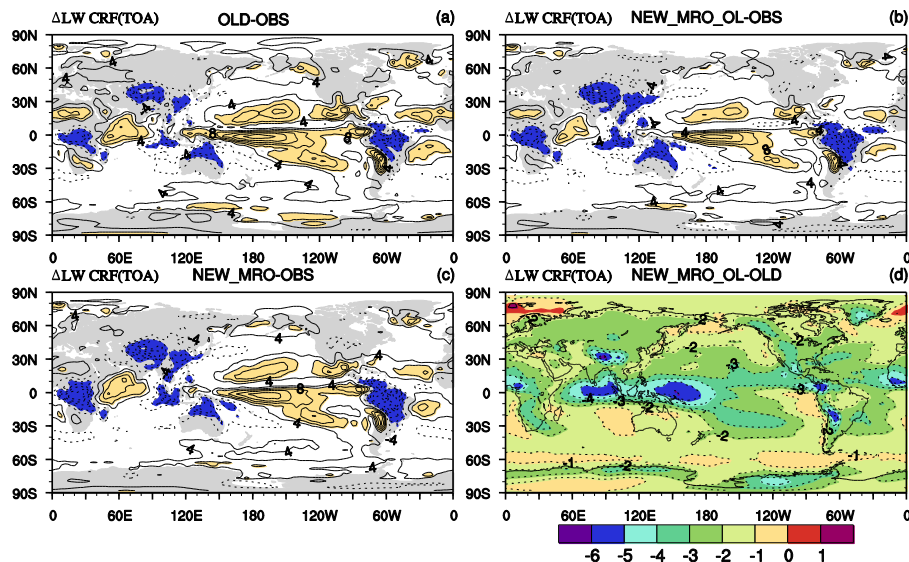
Fig. 3. The annual mean differences in LW CRF among the **(a)** OLD, **(b)** NEW_MRO_OL, and **(c)** NEW_MRO simulations and CERES_EBAF observations with differences larger (smaller) than 8 (−8) Wm^{-2} shaded in yellow (blue). Annual mean differences between NEW_MRO_OL and OLD are shown in **(d)**.
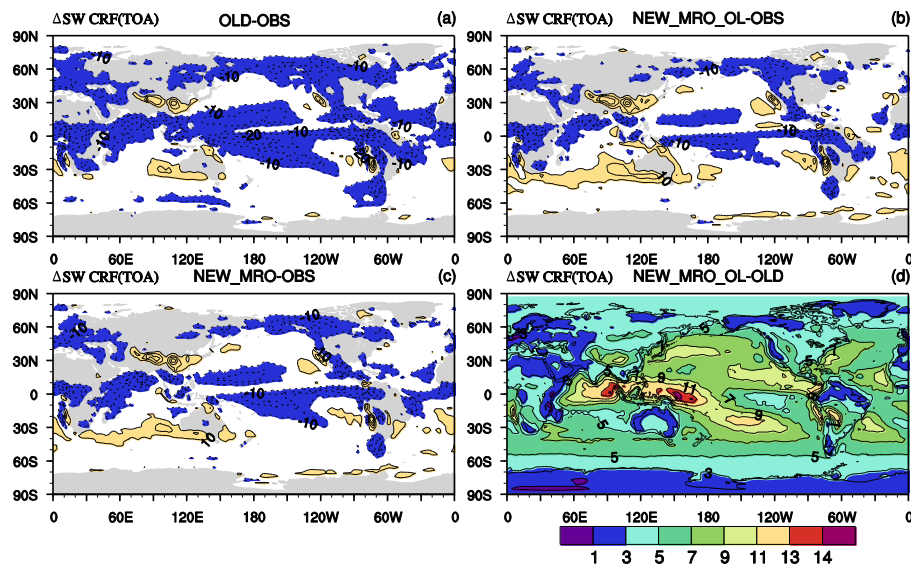
Fig. 4. The same as Fig. 3 but for SW CRF. Differences larger (smaller) than 10 (−10) Wm^{-2} are shaded in yellow (blue) in **(a–c)**.
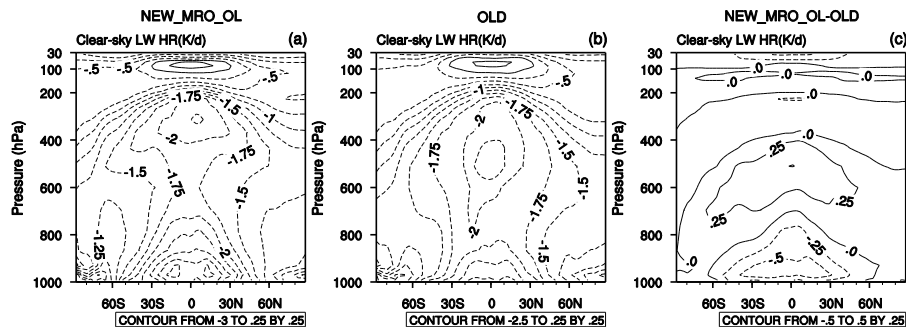
Fig. 5. Zonal annual mean clear-sky LW heating rate for **(a)** NEW_MRO_OL and **(b)** OLD and **(c)** the difference between them.
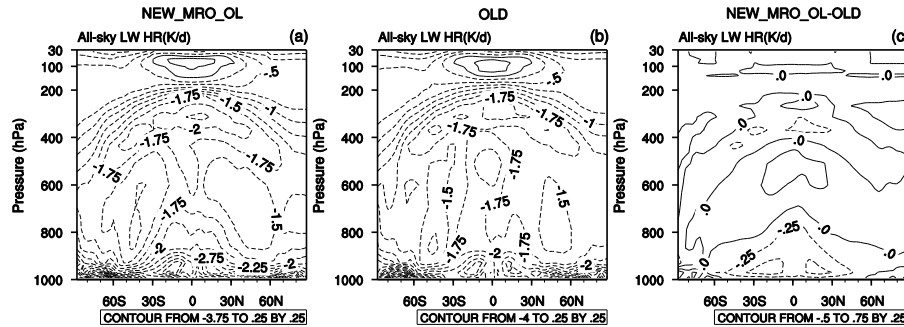
Fig. 6. The same as Fig. 5, but for the all-sky LW heating rate.

Title Page

Abstract | Introduction

Conclusions | References

Tables | Figures

|◀ | ▶|

◀ | ▶

Back | Close

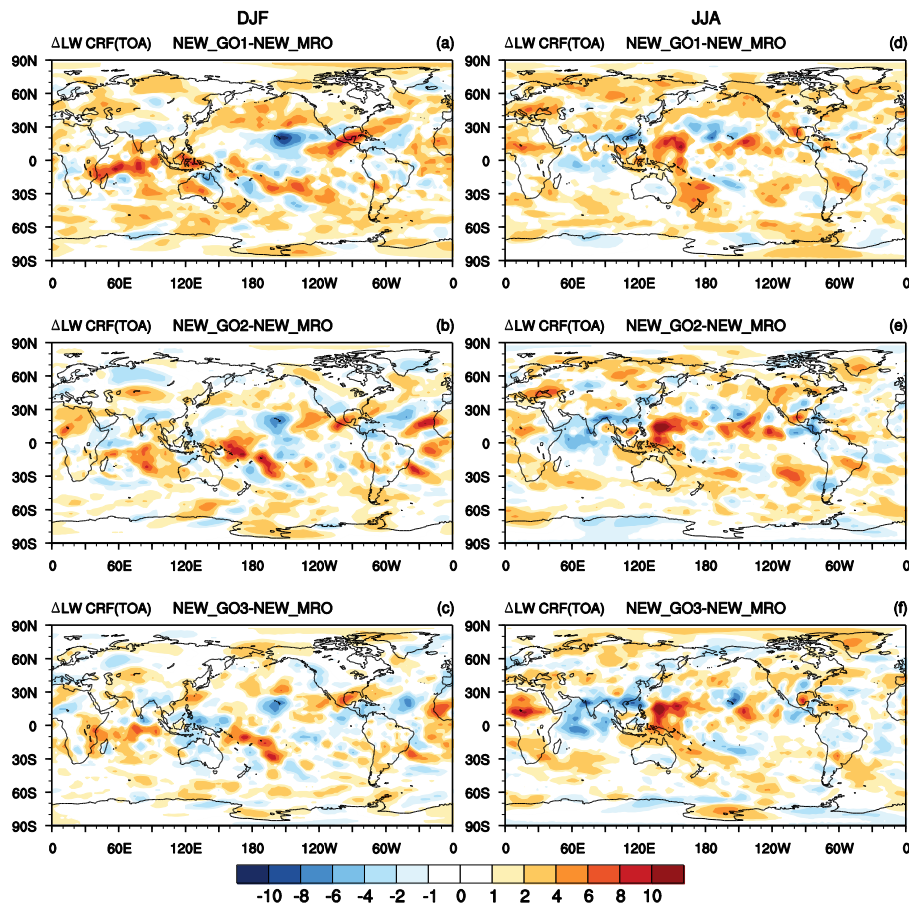Full Screen / Esc

Printer-friendly Version

Interactive Discussion
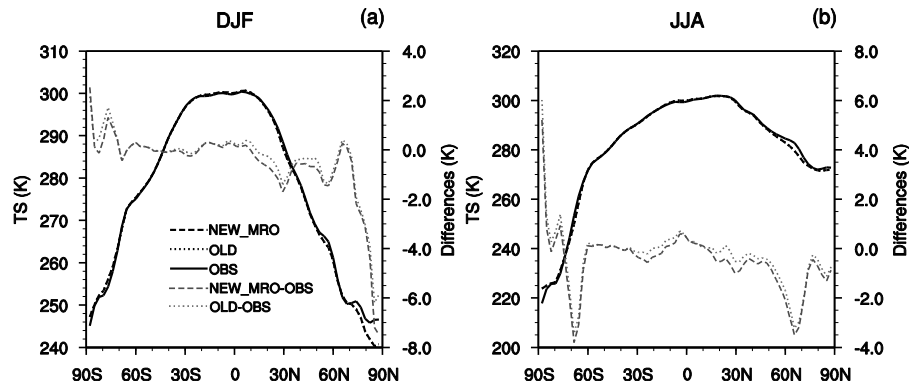
Fig. 7. Zonal mean surface temperature in DJF (left) and JJA (right) from NEW_MRO (black dashed), OLD (black dotted), and ERA-40 reanalysis data (black solid), as well as the differences between NEW_MRO and ERA-40 (gray dashed) and between OLD and ERA-40 (gray dotted).
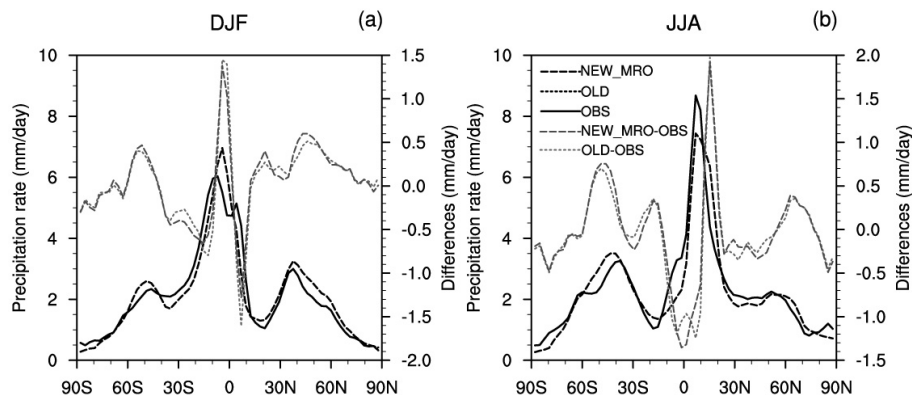
Fig. 8. The same as Fig. 7 but for precipitation rate. The observational dataset is from Xie and Arkin (1997).
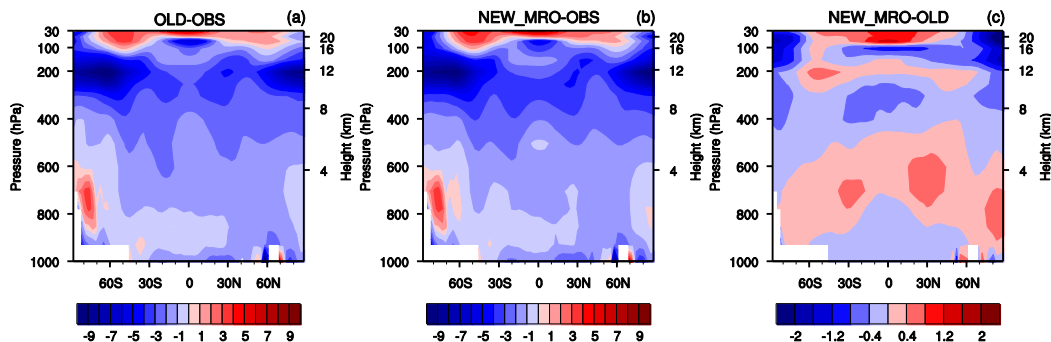
Fig. 9. Biases in zonal annual mean atmospheric temperature compared with ERA-40 reanalysis for **(a)** OLD and **(b)** NEW_MRO simulations and **(c)** the differences between NEW_MRO and OLD.
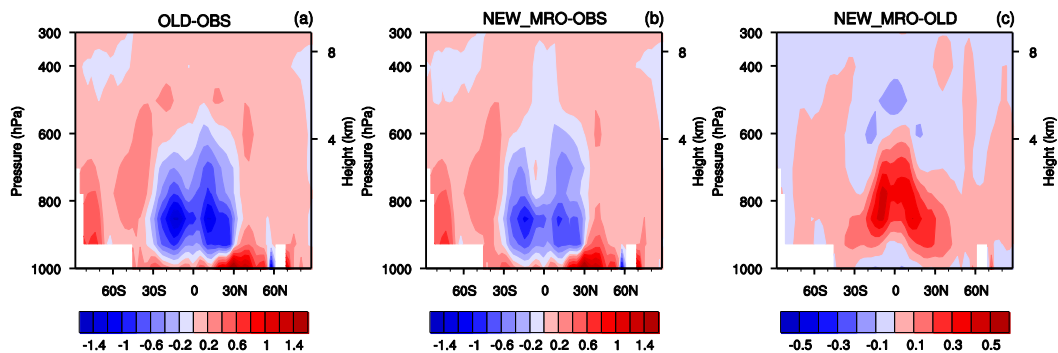
Fig. 10. The same as Fig. 9 but for specific humidity.
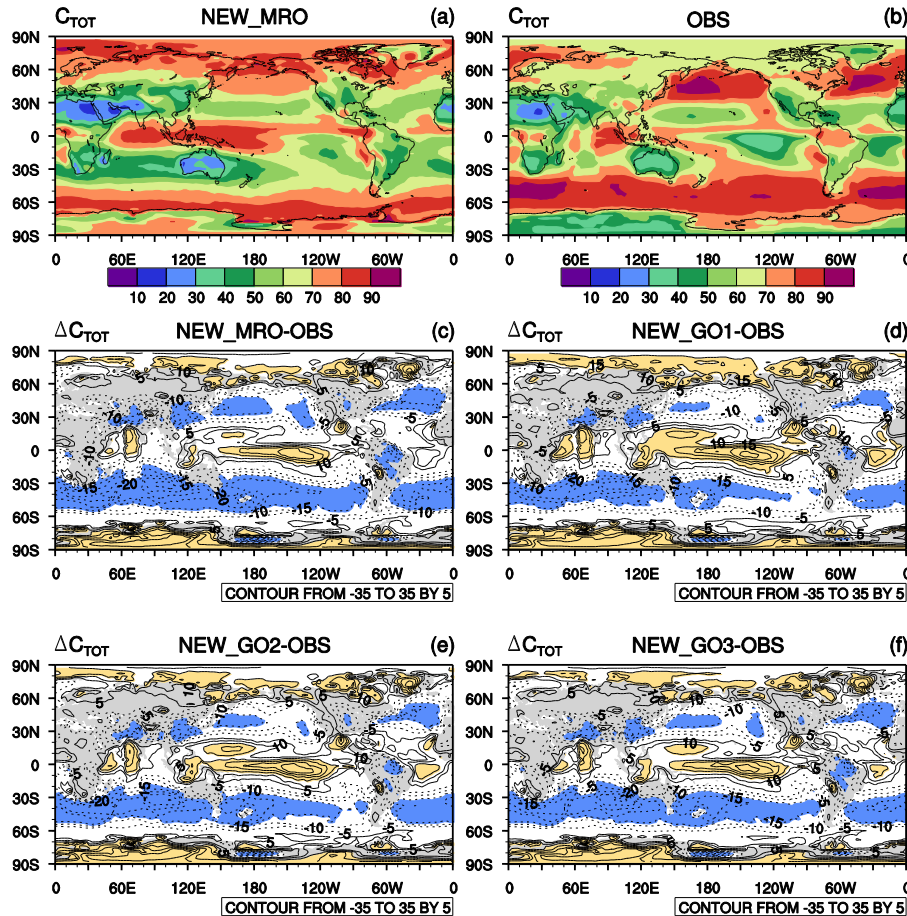
Fig. 11. The annual mean total cloud fraction (C_{TOT}) from **(a)** the NEW_MRO and **(b)** IS-CCP observations and the differences between ISCCP observations and **(c)** NEW_MRO, **(d)** NEW_GO1, **(e)** NEW_GO2, and **(f)** NEW_GO3.

Title Page

Abstract | Introduction

Conclusions | References

Tables | Figures

|◀ | ▶|

◀ | ▶

Back | Close

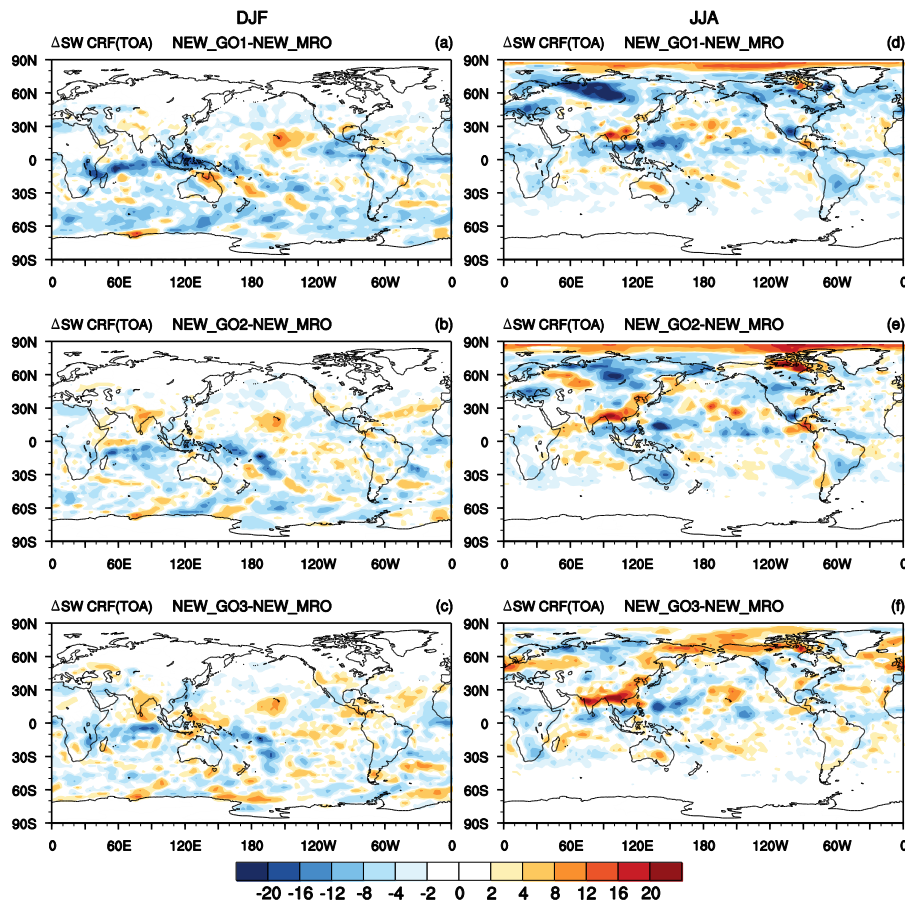Full Screen / Esc

Printer-friendly Version

Interactive Discussion
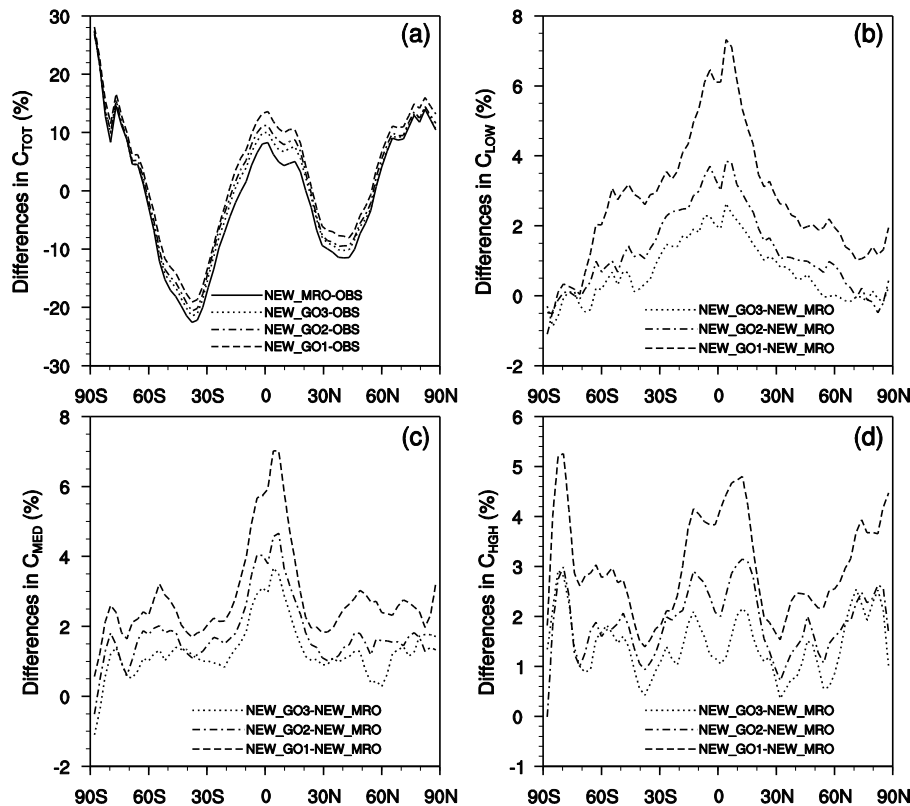
Fig. 12. Differences in **(a)** total cloud fraction between simulations and ISCCP observations and **(b)** low (C_{LOW}), **(c)** middle (C_{MED}), and **(d)** high (C_{HGH}) cloud fractions between NEW_GO1, NEW_GO2, NEW_GO3, and NEW_MRO.

Fig. 13. Differences in LW CRF between NEW_GO1, NEW_GO2, and NEW_GO3 and NEW_MRO in DJF (left) and JJA (right).

Fig. 14. The same as Fig. 13, but for SW CRF.
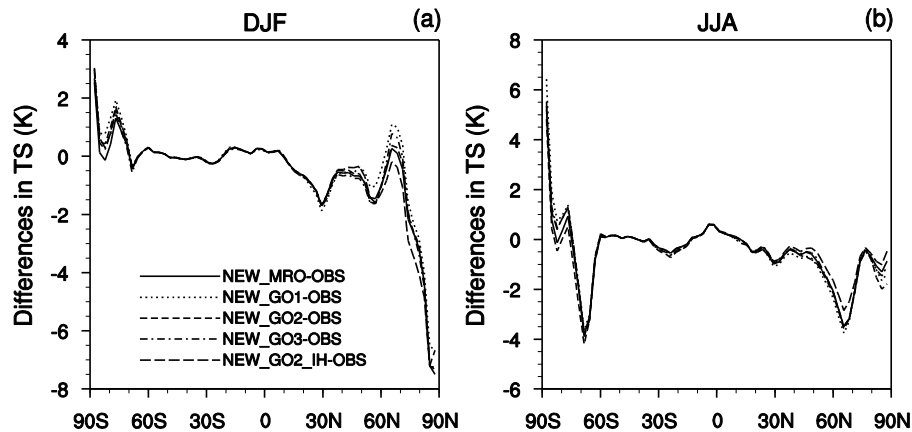
Fig. 15. Zonal mean biases in surface temperature of McICA simulations with different cloud configurations during **(a)** DJF and **(b)** JJA compared with ERA-40 reanalysis.

Full Screen / Esc

Printer-friendly Version

Interactive Discussion
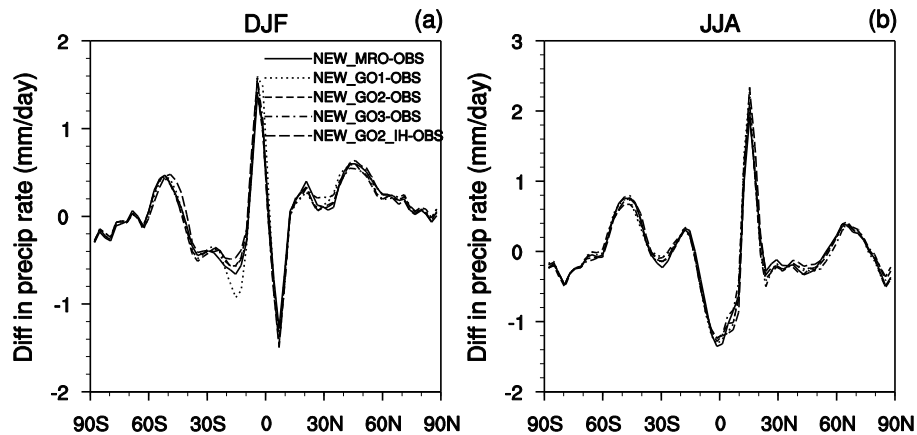
Fig. 16. The same as Fig. 15, but for precipitation rate.
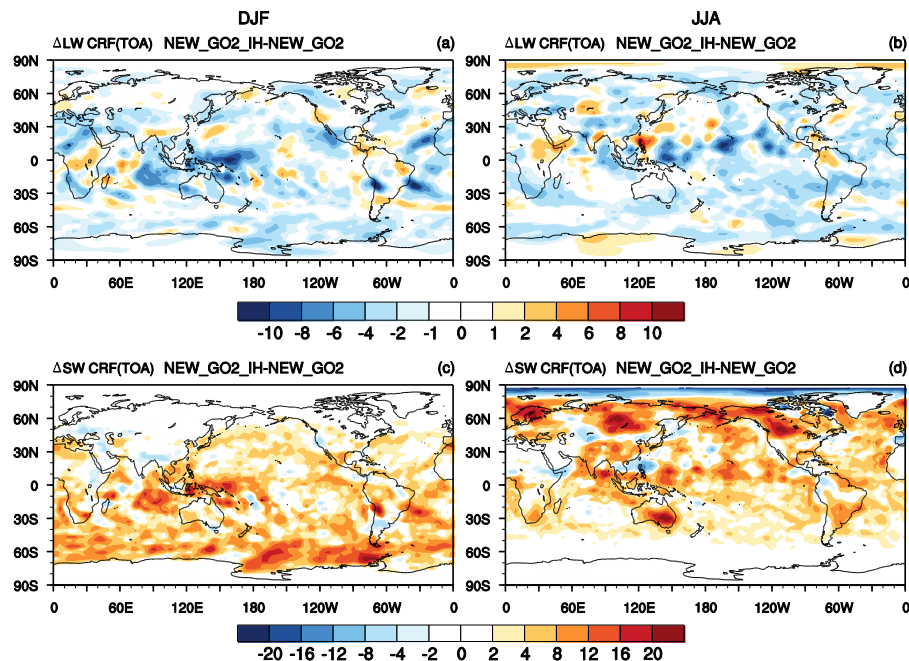
Fig. 17. Differences in **(a–b)** LW CRF and **(c–d)** SW CRF between NEW_GO2_IH and NEW_GO2.

Title Page

Abstract | Introduction

Conclusions | References

Tables | Figures

|◄ | ►|

◄ | ►

Back | Close

Full Screen / Esc

Printer-friendly Version

Interactive Discussion